OPEN ACCESS
IOP Publishing
Nanotechnology

Nanotechnology **34** (2023) 385001 (11pp) https://doi.org/10.1088/1361-6528/acdd09

Deterministic nanoscale quantum spin-defect implantation and diffraction strain imaging

Nazar Delegan[1,2,*], Samuel J Whiteley[3], Tao Zhou[4], Sam L Bayliss[5], Michael Titze[6], Edward Bielejec[6], Martin V Holt[4], David D Awschalom[1,2] and F Joseph Heremans[1,2]

[1] Center for Molecular Engineering, Materials Science Division, Argonne National Laboratory, Lemont, IL 60439, United States of America
[2] Pritzker School of Molecular Engineering, University of Chicago, Chicago, IL 60637, United States of America
[3] HRL Laboratories, LLC, 3011 Malibu Canyon Rd, Malibu, CA 90265, United States of America
[4] Center for Nanoscale Materials, Argonne National Laboratory, Lemont, IL 60439, United States of America
[5] James Watt School of Engineering, University of Glasgow, Glasgow, G12 8QQ, United Kingdom
[6] Sandia National Laboratories, Albuquerque, NM 87123, United States of America

E-mail: ndelegan@anl.gov

Received 27 January 2023, revised 6 March 2023
Accepted for publication 9 June 2023
Published 3 July 2023

Abstract

Local crystallographic features negatively affect quantum spin defects by changing the local electrostatic environment, often resulting in degraded or varied qubit optical and coherence properties. Few tools exist that enable the deterministic synthesis and study of such intricate systems on the nano-scale, making defect-to-defect strain environment quantification difficult. In this paper, we highlight state-of-the-art capabilities from the U.S. Department of Energy's Nanoscale Science Research Centers that directly address these shortcomings. Specifically, we demonstrate how complementary capabilities of nano-implantation and nano-diffraction can be used to demonstrate the quantum relevant, spatially deterministic creation of neutral divacancy centers in 4H silicon carbide, while investigating and characterizing these systems on the $\leqslant$25 nm scale with strain sensitivities on the order of 1×10^{-6}, relevant to defect formation dynamics. This work lays the foundation for ongoing studies into the dynamics and deterministic formation of low strain homogeneous quantum relevant spin defects in the solid state.

Keywords: nanoscale, quantum spin defects, x-ray diffraction, strain engineering

(Some figures may appear in colour only in the online journal)

1. Introduction

Spin defects in large bandgap materials have been demonstrated as an effective platform for quantum information processing, namely for applications in sensing and communication [1, 2]. These point defect qubits, such as the negative nitrogen-vacancy (NV^-) center in diamond [3–5] and neutral divacancies (VV^0) in silicon carbide (SiC) [6–8] have been

* Author to whom any correspondence should be addressed.

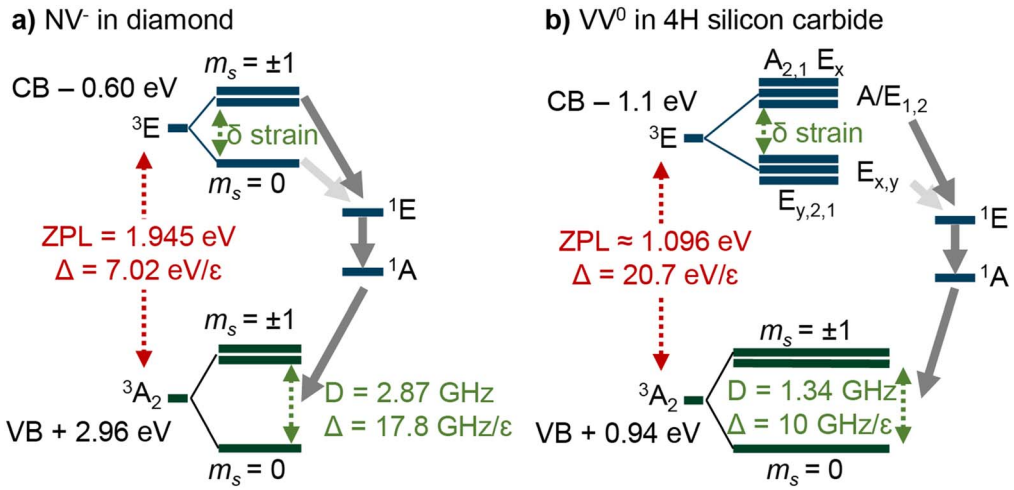

Figure 1. Energy level diagram as a function of strain of a) the NV^- in diamond showing a ~5.75 meV GPa^{-1} (7.02 eV per unit of strain ε) and ~14.58 MHz GPa^{-1} (17.8 GHz/ε) linear dependence for the ZPL and GSS, respectively [36, 37, 39–41]. Calculated with a Young's modulus of 1220 GPa. (b) and VV^0 in SiC as a function of host strain, showing a ≈5 × 10^6 GHz/ε shift for the ZPL [7] and ≈10 GHz/ε for the group state spin-strain susceptibility [48, 49] (25.1 GHz/ε for PL5 [51]).

used to demonstrate record breaking coherence times [9–13], high fidelity quantum gates [14, 15], quantum entanglement and networking at a distance [16–19], and high-sensitivity quantum metrology [20]. These demonstrations are enabled by a spin dependent optical readout mechanism resulting from spin-photon manifolds as shown in figures 1(a)) and (b) for the NV^- in diamond and VV^0 in 4H-SiC, respectively. These defect mid-gap electronic energy structures allow for easy spin initialization and read-out via an intersystem crossing, while being energetically separated from the host's energy bands, resembling isolated atomic systems. While this approximation is quite convenient, in truth, the defect energy level structures are intrinsically sensitive to their local charge, magnetic, crystallographic symmetry, and strain environments—all of which can have varied and hard to systematically quantify effects on the spin-defect's quantum performance [2]. Because of this inherent variability, many of the state of the art demonstrations have relied on pre-screened defects, hand picking the qubits that showed the best properties for the intended experimental demonstration—spin-defects that had well understood and pre-selected local charge, spin, crystallographic, and strain environments. Much research effort has been placed into overcoming this selection bias using a number of varied methods of deterministically synthesizing quantum information science (QIS) relevant spin defects in large bandgap materials [2] while controlling and understanding the qubit relevant environmental parameters. Unfortunately, incorporating these defects into devices still presents challenges as growth, defect spin creation, and device fabrication methods generally degrade the qubit properties [21–24]. While this is a multifaceted problem, for the purposes of this work, we will focus on the role that crystallographic distortions and defects in the host material play in this degradation of spin-defect properties.

Crystallographic features such as stacking faults, twin boundaries, glide planes, and grain boundaries result in locally varied strain profiles and reduced lattice symmetries which play a significant role in the local electrostatic environment around quantum point defects. These features can often adversely affect the properties of the quantum system, but potentially also present a unique opportunity to serve as a means of tuning optical properties, addressability, and protect coherence [12, 25, 26]. Furthermore, the relevant $\leqslant 1$ μm length scale of these spin-defect/crystal-defect systems makes it difficult to discern the exact origin of the local distortions. While damage in monocrystalline semiconductors, including threading dislocations, stacking faults, and point defects can appear localized, the strain gradients that they impart can span tens of micrometers.

Such extended crystallographic defects arise from many sources, including (1) host-material synthesis, (2) sample preparation and nanofabrication, and (3) *ex situ* defect creation. Dislocations, stacking faults, and twin boundaries can often arise through growth synthesis methods such as in chemical vapor deposition of diamond [21, 27] and SiC [28, 29]. Surface smoothing techniques using chemical mechanical polish are suspected of creating sub-surface microfractures within the crystal that can persist several micrometers into the material [30]. Furthermore, spin-defect generation techniques via ion implantation and electron irradiation [2, 31] typically rely on thermal post-processing to achieve spin-defect creation efficiency and lattice 'healing' with very little quantitative understanding of the process at local and intermediate length scales (≈10 nm to 1 μm). The effects of these crystallographic features on the spin-defect to host-material relationship remains poorly understood due to their inherent complex and local nature. This has motivated a number of recent advances in the field, attempting to address these issues—notably using state-of-the art focused ion beam nano-implantation techniques for deterministic creation of spin-defects in conjunction with highly coherent nanoscale focused x-ray techniques as a means to probe these quantum relevant nanoscale phenomena. Single defect creation nano-

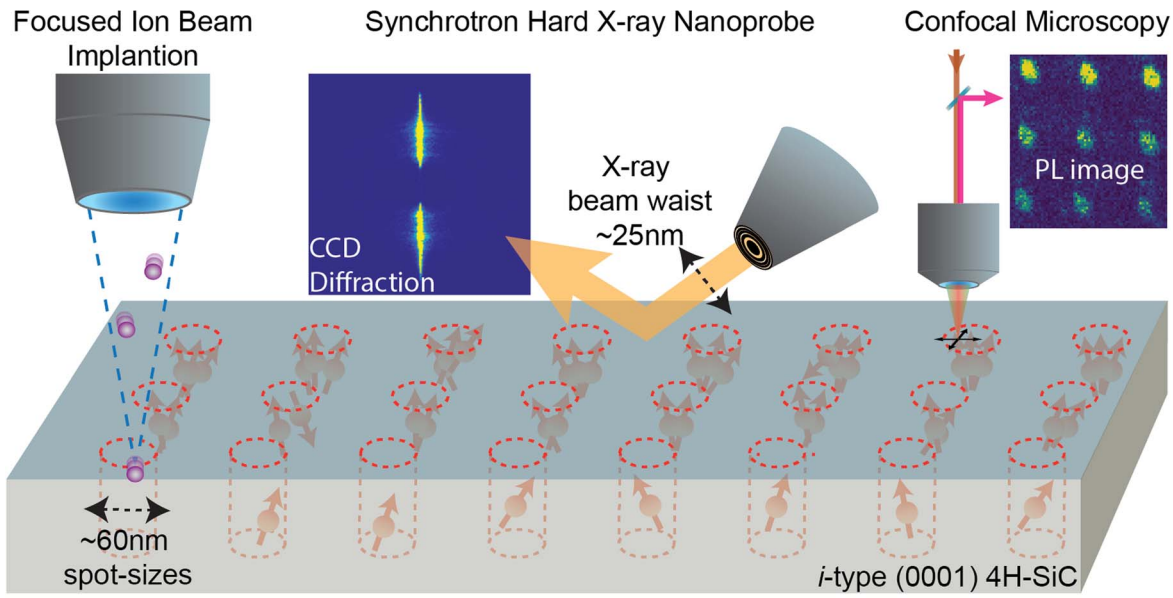

Figure 2. Summary of experimental set-up, combining Focused Ion Beam (FIB) nano-implantation (defect creation), Hard x-ray Nanoprobe (HXN) nano-diffraction (spatial strain mapping), and confocal 8 K infrared Photoluminescence (PL) characterization.

implantation capabilities have been demonstrated at the Center for Integrated Nanotechnologies at the Department of Energy's Sandia National Laboratories. Whereas strain sensitive x-ray imaging, capable of non-destructive local 3D strain imaging with nanoscale ($\leqslant$25 nm) resolution, has been demonstrated with the Hard x-ray Nanoprobe (HXN) at the Department of Energy's Advanced Photon Source (Argonne National Laboratory) and the Center for Nanoscale Materials. These versatile tools have enabled a number of recent advances in understanding the structural dependency of spin qubit/host systems and methods to improve and harness the local crystallographic environment of these quantum systems.

The objectives of this work are threefold. Firstly, we summarize several recent results pertaining to how crystallographic defects and strain dictate solid-state spin-defect performance while highlighting the broad benefits of understanding and controlling such phenomena for quantum relevant material systems. Secondly, we introduce nano-implantation and HXN capabilities available within the U.S. Department of Energy's Nanoscale Science Research Centers, while highlighting several recent results made possible with such capabilities (figure 2). Thirdly, we demonstrate these elements in the context of ongoing quantum relevant works into quantum defect synthesis. Specifically, we will discuss deterministic creation of VV^0 in 4H-SiC and characterization on the $\leqslant$25 nm scale with sensitivities relevant to defect formation dynamics.

2. Methods

The samples studied are Norstel AB *i*-type epitaxial on *i*-type bulk 20 μm thick 4H-SiC (nominal *c* lattice constant of 1.0085 nm) with a $\approx$4° miscut towards the $\langle 11\bar{2}0\rangle$ direction as determined by the mother-wafer major flat. These samples had Ti/Au alphanumeric fiducials deposited to serve as alignment markers for subsequent steps and were then diced.

The smaller substrates were nano-implanted with Si^{++} ions at 200 keV, focused down to 66 $\times$ 56 nm^2 spot size (as measured during nano-implantation) with fluences of 10000, 5000, 1000, 500, 100, 50, 20, 10 ions/spot with a 1 μm pitch (fluence was varied in rows, whereas columns were used for statistical repeatability). The implantation was done at an incidence angle of $\approx$7° to avoid channeling. Thereafter, each chip was split into two identical sides with half left as is for subsequent characterizations, whereas the other half underwent thermal processing at 850 °C for 30 min under a flowing Ar atmosphere.

The samples were investigated with a pencil-like x-ray beam of $\approx$25 nm waist with a $\lambda = CuK_\alpha$ energy of 8.04 keV at the 4H-SiC (0004) diffraction condition of $2\theta \approx 35.3°$ with a sample $\theta = 21.80°$ along the scan *x*-axis with $\approx$25 nm steps in both *x* and *y* directions via locked hybrid sample motors. The x-ray nano-diffraction was performed under 10^{-6} Torr vacuum with $\approx$8 h thermal stabilization at room temperature between sample mounting and alignment to minimize thermal drift. Strain resolution is quantified at $1 \cdot 10^{-4}\frac{\delta c}{c}$ with a detection limit of $1 \cdot 10^{-6}\frac{\delta c}{c}$ (change in the two-dimensional counts diffraction location) with the resolution given by a Si_{111} monochromator with $10^{-4}\frac{\delta E}{E}$ bandpass (location accuracy of the two dimensional projection size of far field detected counts).

Photoluminescence (PL) mapping of the sample was done in a home-built cryogenic confocal microscope using off-resonant 905 nm excitation and operating at 8 K. The PL was separated from the excitation using long-pass filters and detected with a fiber-coupled superconducting nanowire single-photon detector (SNSPD).

3. Body

Early quantum centered investigations of solid state spins often circumvented discussions of crystallographic and environmental inhomogeneity via selective pre-screenings of the available qubit defects. While effective for proof-of-concept or fundamental solid-state studies, this approach is incompatible with scaling quantum information science into a robust technological platform. When considering the entire set of point-defects for desired quantum properties, there are often large sample-to-sample and inter-sample variations that are not fully explained. These properties include optical stability, charge stability, and spin coherence as detailed in other reviews [2, 32, 33]. While the relation of certain aspects of dopant concentration, overall crystal quality, and damage caused by ion implantation and irradiation damage are reasonably well correlated—there remain a number of less understood phenomena that are often invisible to common characterization that contribute to defect-to-defect variability. Recent efforts have begun to address these inconsistencies, with studies focusing on the effect of bulk host material defects [34], surface related effects [30, 35], and processing related damage [22] on qubit coherence times, spectral homogeneity, and charge stability.

The electronic structure of point defects is intrinsically tied to the isotropic and anisotropic strain profile of their host matrices [36–38]. The isotropic dependence, at its simplest, translates to a linewidth broadening for ensembles [37] and a quantifiable shift in the single defect energy levels as a function of strain, as shown in figures 1(a)) and (b) for the NV^- center in diamond and the VV^0 in 4H-SiC, respectively. Indeed, taking the example of the NV^- in diamond with inherent C_{3v} symmetry and a quantization axis along $\langle 111 \rangle$ (figure 1(a))), both the zero phonon line (ZPL) and the ground-state splitting parameter D are tied to their local isotropic strain, with a $\approx$5.75 meV/GPa (7.02 eV per unit of strain ε) and $\approx$14.58 MHz/GPa (17.8 GHz per ε) linear dependence, respectively [36, 37, 39–41]. More accurately, strain perturbations in the host lattice translate into variations of the Jahn-Teller symmetries, resulting in non-uniform shifts of the defect's various energy levels [38, 42]. These anisotropic effects on the various excited and ground state optical transitions can be deconvolved into their independent components (e.g. longitudinal vs transverse) and tied back to their respective effects on the spectral diffusion in a dynamic environment and optical transition shifts [35]. In a similar vein, the VV^0 center in 4H-SiC has four distinct crystallographic sites that each present their own unique optical and strain characteristics (with additional spectrally identified configurations attributed to stacking fault-like defects [43]), where the sites generally share a characteristic energy level structure shown in figure 1(b)) [44]. Most investigations have focused on axial VV^0 centers (i.e. *kk* and *hh*) due to their higher symmetry [15, 44–46]. However, owing to their lower symmetry and anisotropic crystal field splitting, basal VV^0 (i.e. *kh*-VV^0) demonstrate higher effective ground state splitting E (which could also be achieved with applied strain to higher symmetry point-defects) and as such have been used to demonstrate decoherence protected subspaces via dressed states (microwave driving of a VV^0 clock transition) [12]. This was exploited to obtain T_2^* and T_2 times of 22 ms and 64 ms, respectively. Reinforcing that deterministic strain engineering of defects holds a lot of promise for a variety of quantum information platforms. There have been limited studies of the excited state orbital to strain coupling in SiC defects. The ZPL strain susceptibility is approximately 10^6–10^7 GHz/ε calculated from optical spectroscopy measurements on divacancy ensembles [7, 39]. While studies are lacking, the VV^0 excited states are expected to have the same order of magnitude interactions as the NV in diamond [47–49]. These strain modifications hold an upper bound unique for each defect system. Simply put, the applied pressure must not alter the defect's configuration such that it loses its symmetry group, and by extension its spin-photon manifold and energy structure. For NV centers in diamond, this breakdown of the optical spin contrast was observed at strains above $\approx 4 \cdot 10^2$ ($\geqslant$48 GPa) [50], whereas for VV^0 in 4H-SiC this value was closer to $\approx 9 \cdot 10^2$ ($\geqslant$40 GPa) [51].

Sample-scale strain variations are relatively easy to characterize with commonly available x-ray diffraction experiments. However, local crystallographic defects (e.g. stacking faults, screw dislocations, etc) can create abrupt changes of strain profiles, resulting in significant local discontinuities of electrostatic environments. Few characterization tools are available to spatially map these local strain profiles and by extension, understand the magnitude of their effect on the point-defects they influence. Additionally, crystallographic anomalies act as local scattering objects, negatively affecting mechanical driving fields that are critical for many quantum systems [35, 52]. Only recently have state-of-the-art, nanometer scale crystallographic characterization tools, such as the HXN, began to reveal commonplace features as seen in figures 3(a)) and (c) - showing a dislocation in 4H-SiC obtained with HXN raster scanning, revealing local strain variations of $1.1(0.1) \cdot 10^{-4}$ over 0.28 μm. It is worth mentioning that while large, this detected strain is likely quantitatively underestimated due to the depth convolution of the strained features (depth projection) and pristine material interacting with the XRD beam [53]. In other words, the quoted value is likely a lower bound, a more exact value could be obtained with a multi projection analysis that would require multiple (at-least partially orthogonal) diffraction conditions [54]. Even at this lower bound for the observed strain, two VV^0 located at P1 and P2 (See figure 3(c))), assuming isotropic strain, would present a spectral shift of $\sim$2.4 meV and $\sim$1.14 MHz, for the ZPL and ground state splitting, respectively, while being strictly within a single diffraction limited photoluminescence spot size. Similarly, clover-shaped dislocation defect features are also regularly found in CVD grown diamond with the HXN [54]. Such features were noted with strain variations of $\approx 2 \cdot 10^{-4}$ over $\approx$0.20 μm. Practically speaking, two NVs sharing the same diffraction limited optical spot within that particular defect's zone of influence, would present 1.4 meV and 3.6 MHz shifted ZPL and D values, respectively. Optimal lifetime-limited optical linewidths are quoted to be 11(5) MHz [13]

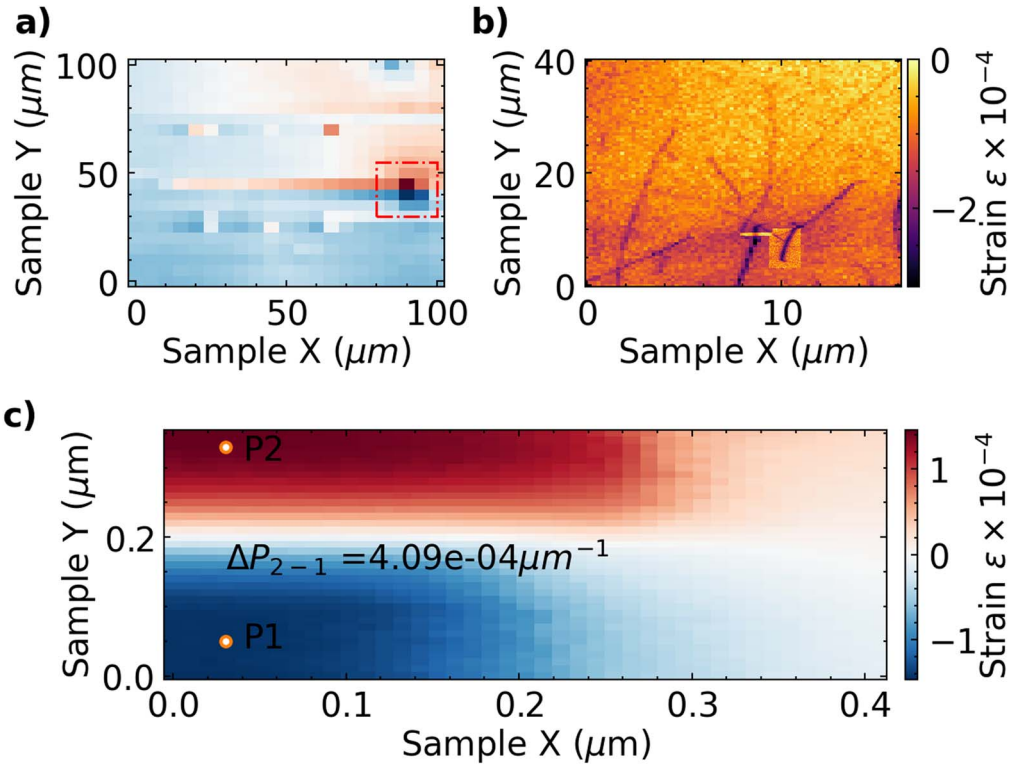

Figure 3. (a) HXN 2D coarse motor scan of a region of interest on a 4H-SiC sample (as seen by the presence of alignment markers) with 5 um step sizes on the left figure, showing the start and extent (∼100 micrometers) of a defect consistent with a screw dislocation signature. (b) Composite HXN scan of a 4H-SiC 'clean' region, taken during a screening scan, showing sub surface crystallographic defects extending both in the bulk and laterally. Scans are performed in low resolution mode (∼0.5 μm steps) for most of the data except in the ∼7.5 to 10 μm area where 3 high resolution scans (∼50 nm steps) are aligned and superimposed to show observed features in better detail. Observed features are of tensile nature (negative strain). (c) A ∼10 nm step size, high-resolution raster nano-diffraction scan of the region approximately outlined in the low-resolution scan of (a). Color bar applies to both (a) and (c). We note a drastic change of strain from tensile to compressive, showing a 1.14 $\cdot 10^{-4}$ ε variation in strain over 0.28 μm.

and 13 MHz [55] for the VV^0 and NV^-, respectively, whereas observed linewidths are typically closer to 20–200 MHz and 30-400 MHz, respectively. It is not unreasonable to propose that a large variation of defect characteristics in a given material result from the host's crystallographic defects, which are found on the order of $\geqslant 10^3\,\mathrm{cm}^{-2}$ (for thicknesses of 500 μm) for both homoepitaxial diamond and 4H-SiC [56–58]. While some of these are intrinsic to the material growth process [21, 29], others result from the processing and fabrication of the quantum defects, devices, and other surface treatments themselves [22, 30] as seen in figure 3(b)). The ubiquitous and sparse nature of these defects can result in undetectable outliers, establishing the need for x-ray microscopy at this scale.

The intrinsic sensitivity of point-defects to their host environment makes qubits like the NV^- center excellent embedded vectorial strain sensors [22, 34, 54, 59]. Indeed, in combination with state-of-the-art nano-scale x-ray diffraction experiments, they have even been proposed as a viable path for dark matter detection [54, 60]. However, for applications such as quantum networking, where most schemes rely on frequency matched photon generation, this defect-to-defect variation is highly undesirable and cannot always be compensated for with DC voltages via device electrodes [16, 17, 61]. In fact, low strain/E field sensitivity is in part what motivates research into defects with increased symmetries (e.g. group-IV defects in diamond [62]) as these color centers present group theory dictated symmetrical behaviors that are, to the first order, insensitive to local variations in electric and strain fields. These challenges are amplified for more advanced schemes such as nanophotonic structures [45] or near-interface reliant devices and sensors [63]. As such, this escalates the undesired dependence on any interface and fabrication related effects. Regardless, for most quantum relevant defect systems, the variability in local strain and host material environments needs to be well understood [2, 38]. Fundamentally, this would allow for a quantitative understanding of defect-to-defect variability, which can then be compensated for in applications that require it.

Most intriguing is the idea of utilizing local crystallographic defects to engineer unique defect systems and devices. Considering two theoretical point-defects located on either side of the stacking fault in figure 3(c)), we can approximate that these two defects will have their spectral signatures shifted sufficiently to enable sub-diffraction limited independent addressability, paving the way for a slew of advanced quantum relevant control schemes. Indeed, this is a naturally occurring palette for local structure-function engineering and characterization. Or, in the case of defects such as the group-IV-vacancy family of defects in diamond [62], local

strain engineering can be used to improve the coherence times and/or operation temperature of the defects. Simply put, by increasing the ground-state splitting to values where the phonon population is significantly reduced, the main decoherence mechanism, i.e. the electron-phonon interaction in the split-vacancy centers, can be suppressed. This has been demonstrated for SiV^- centers in diamond, where 10^{-4} strain was used to increase the ground state splitting from 46 to $\geqslant$500 GHz, resulting in a significant increase in coherence times, alternatively equivalent to increasing the operation temperature (while maintaining coherence times fixed) of the defects from 100 mK to 4.2 K [63, 64]. Using a similar approach, but aimed at spectral alignment, GeV^- ground state splitting strain tuning of ~100 GHz was demonstrated, extracting excited and ground state splitting variations of 2.8 PHz/ε and 2.2 PHz/ε, respectively [65]. These techniques are limited by the eventual degeneration of the defect's symmetry group of D_{3d} being reduced to lower forms such as C_2 or D_2 point groups.

Overall, control of local lattice perturbations near optically-active spin qubits remains a key component towards improving coherence and harnessing the full potential of hybrid architectures. The deleterious effects of crystallographic distortions within the host lattice from the perspective of optically active defects remains relatively unexplored. Techniques capable of probing the host material strain and crystallography on the nanometer scale are highly desirable for both quantum and classical technological applications. In this context, the HXN at Argonne's Advanced Photon Source and Center for Nanoscale Materials of the Department of Energy's Argonne National Laboratory is a unique and versatile characterization platform, enabling groundbreaking experiments in both classical and quantum applications [52–54]. The basic set-up of HXN characterization relevant to the rest of this work is presented in figure 2. The instrument scans a focused monochromatic x-ray beam on the surface of a sample while simultaneously collecting x-ray diffraction (XRD) and when applicable, x-ray fluorescence (XRF), as well as x-ray excited optical luminescence (XEOL) signal. A two-dimensional map is typically obtained with a sub-25 nm spatial resolution of (limited by the spot size of the focusing optics) and a strain resolution of better than 10^{-4} $\frac{\partial c}{c}$. Depth information is obtained with either geometrical projections [54] or coherent imaging techniques [66], the latter has the additional advantage of an improved 6 nm spatial resolution [67]. In order to maintain the sub-25 nm spatial resolution, the instrument operates under high vacuum, with optional sample environments such as electrical biasing (up to 100 V DC or 10 V RF), cryogenic cooling (~70 K), and optical pumping.

In related works, the HXN was used in stroboscopic scanning x-ray diffraction microscope (SXDM) mode, as a means to image real-space dynamic strain within 4H-SiC [52]. In that demonstration, SXDM was used to correlate strain waves with photoluminescence measurements from optically-active divacancy defects in 4H-SiC. The pulses from the synchrotron storage ring were synchronized to the frequency of the surface acoustic wave launchers. For the purposes of this paper, the deterministic synthesis of divacancies in 4H-SiC was quantitatively studied using the HXN, in combination with PL microscopy enabled by state-of-the art nano-implantation based synthesis at the Center for Integrated Nanotechnologies (CINT) of the DOE's Sandia National Laboratories. Nanoimplantation is available for ions from approximately 1/3rd of the periodic table with landing energies from <1 keV up to 200 keV with targeting resolution < 50 nm. Additionally, *in situ* electrical and optical implantation feedback is available allowing deterministic ion implantation and formation of single photon emitters [68]. The objectives of these ongoing efforts are threefold: (i) demonstrate deterministic synthesis of VV^0 in 4H-SiC, (ii) characterize the implantation induced strain as how it relates to the defect formation process, and (iii) optimize optical defect formation via tailored thermal processing.

The samples studied herein are 20 μm thick epitaxial undoped 4H-SiC layers on a high purity semi-insulating bulk wafer, grown by Norstel AB. These single crystal chips have a nominal c lattice constant of 1.0085 nm. The samples were nano-implanted at a 7° incidence angle (to avoid channeling) with Si^{++} ions at an effective energy of 200 keV, which were aligned to Ti/Au fiducial alignment markers, with the implantation pitch being 1 μm. Stopping and Range of Ions in Matter (SRIM) software simulations indicate that the implantation spots should have resulted in a ~180 nm deep nano-implanted pear-shaped spots with a small average straggle radius of 43 nm quasi-isotropic from the implantation center. The implantation zones were composed of approximately 5 to 30 identical implantation columns (for statistics) and fluence arrays starting at 10000 ions/spot and decreasing all the way down to 10 ions/spot (i.e. 10000, 5000, 1000, 500, 100, 50, 20, 10). While typical highly focused implantation capabilities of the FIB based nano-implanter at CINT achieves implantation spot sizes of 20 × 20 nm^2, due to calibration drift, our implantation spot sizes were quantified that day to be 66 × 56 nm^2. The implanted 4H-SiC sample was split into two chips, and one chip was thermally treated at 850 C for 30 min in an Ar atmosphere.

The samples were investigated at a temperature of 8 K using off-resonant 905 nm laser excitation photoluminescence (PL) as shown for both the annealed and unannealed implantation array in figure 4(a)). Figure 4(a)) shows that similar PL count rates were achieved at 66 mW to 4 μW excitation laser power for the unannealed and annealed samples, respectively. We note that annealing at 850 C in Ar has resulted in a significant increase of VV^0 PL [7, 69, 70]. This can be attributed to the diffusive mobilization of implantation generated silicon (V_{Si}) and carbon (V_C) vacancies [7, 71]. Most of the PL increase is assigned to the formation of additional divacancy centers. Unlike V_C and V_{Si}, which are mobile above ~700 °C [69, 70, 72, 73], divancancies are not expected to dissociate nor mobilize below ~1400 °C [69]. Additionally, vacancy mobilization results in 'lattice healing', i.e. annihilation of vacancies with interstitial species, other defects, and surfaces, resulting in the noted reduction of observed strain, contributing positively to nearby

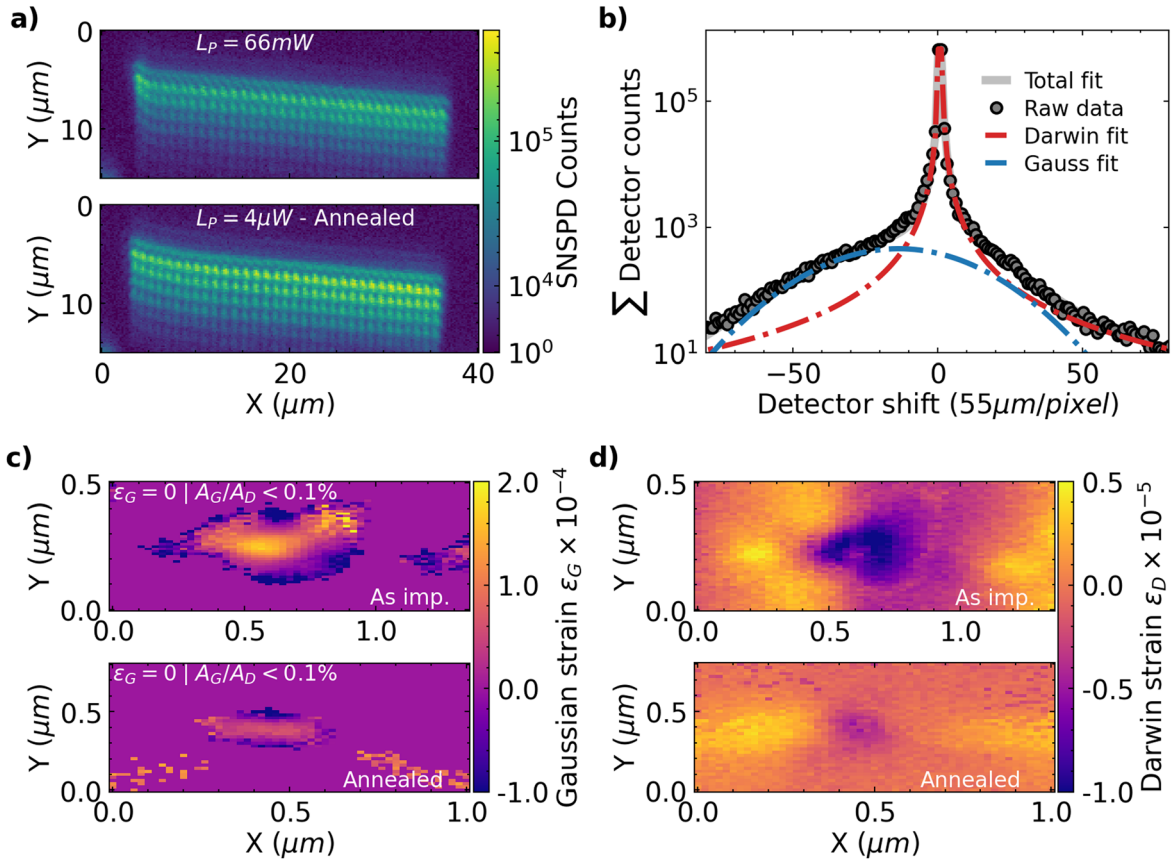

Figure 4. (a) PL of VV^0 obtained via Si^{++} implantation of 4H-SiC with 10000, 5000, 1000, 500, 100, 50, and 20 ions/spot per row organized from top to bottom (10 ion/spot fluence is too faint to observe here), columns are repeated for statistics, nano-implantation pitch is 1 μm. The implantation array curvature is due to experimental error, resulting in initial array drift during implantation. (b) Example of two component quantitative strain fitting model—the Darwin component is representative of the bulk 4H-SiC dynamical diffraction signal [75] and the Gaussian component is assigned to the nano-implantation damaged region (that still maintains sufficient lattice periodicity to diffract, i.e. fully damaged regions are 'invisible') 9c) 2D tensile strain ε profile extracted from the Gaussian component of the two-component fitting model for a 10^4 ion/spot implantation with the as implanted spot showed above and the annealed spot below. The strain is set to 0 when the area of the Gaussian component is $< 0.1\%$ of the Darwin component d) strain response of the host 4H-SiC crystal extracted from the Darwin component for the as implanted spot above, and annealed sample below. It needs to be noted that the interaction volume from the Darwin and Gaussian components differ greatly and as such the extracted strain cannot be compared directly numerically, but can be considered qualitatively.

VV^0 PL emission [74]. While many questions remain and these optical studies are still ongoing, this work demonstrates spatially deterministic VV^0 ensemble creation in 4H-SiC. Lower ion fluences did not reveal single VV^0 with expected count rates (PL count rates compatible with single VV^0 formation) from prior work, which may have been due to charge state instability from excessive local damage caused by implantation or insufficient thermal processing. More work is required to achieve deterministic single VV^0 creation by optimizing the implantation conditions, ion species, and spectroscopy using multiple laser wavelengths for charge repumping.

To better understand how the implantation induced strain and thermal processing is affecting the defect formation process, these arrays were investigated via the HXN in rastering mode. The diffraction peak investigated was the (0004) peak with the beamline photon energy set to match the CuK_α emission line with an energy of 8.04 keV (wavelength of 1.5406 Å). The beam was focused down to an effective pencil beam width of ~25 nm and rastered across the area of ~0.5 μm by 1.3 μm with steps of ~ 25 nm. The obtained data is a full 2D detector diffraction per spatial pixel of the sample projected along the direction of the exit beam [53] which was then collapsed (y-axis counts summed) and annulus normalized as to obtain a quantifiable signal. A two component model was chosen to represent the nano-implanted areas, with a Darwin component representative of the pristine 4H-SiC bulk (limited by dynamical effects) and a Gaussian component representative of the diffracting areas of the nano-implantation spot as seen in figure 4(b)) [53, 75]. Each of the spatial pixels is systematically fitted to this composite model, extracting the 2D strain profile of the implantation spot as shown in figure 4(c)). In addition, to obtain a full picture of how the 'bulk' substrate is responding, the Darwin strain contribution is plotted in figure 4(d)).

From figure 4(b)), we can note that the typical Darwin component contribution is about 2-3 orders of magnitude greater for the 10000 ions/spot scan, increasing to a 4–5 order

magnitude difference for the lower implantation fluences (not shown). Calculating the Bragg extinction depth, we arrive at a Darwin component interrogated depth of ∼5.6 μm, i.e. 99% diffraction signal cutoff depth for (0004) diffraction in 4H-SiC [75]. As such, the Darwin and Gaussian components are interacting with vastly different volumes of the sample. This is reiterated with the SRIM predicted nano-implanted volume of ∼86 nm in diameter and the two dimensional implantation strain data presented in figure 4(c)) (as implanted sample), showing an implantation area volume of ⩽132(7) nm in diameter (Gaussian FWHM of *y*-axis data slice through the strain maximum). From this, a direct quantitative comparison of the strain arising from the Gaussian and Darwin component is difficult without normalizing for the x-ray volumetric interaction. The Darwin component will vastly underestimate strain as it is interacting with microns of pristine 4H-SiC material, whereas the Gaussian component is interacting with a ∼100 nm diffracting volume at the nano-implantation location, but ignoring any areas that no longer diffract due to a catastrophic breakage of periodicity.

Comparing figures 4(c)) and (d) (as implanted), we note that a phenomenological picture emerges, with a tensile nano-implanted core, surrounded by a compressively compensating bulk with peak local strains of about $2 \cdot 10^{-4}$ and $1 \cdot 10^{-5}$, respectively. While still about an order of magnitude away from where optical contrast breakdown is expected [51], the drastically increased strain in the as implanted samples is likely contributing to the difference in PL observed between the as implanted and annealed samples. Given that the scans are performed with a tilted x-ray beam relative to the *x*-axis, the depth information is projected onto the horizontal field of view in the data, as we scan from right to left, shallower features are shifted leftwards as compared to deeper features, indicating that the implantation area is symmetric based on the lack of symmetry in the *x*-axis when going from right to left. Most interestingly, we note two effects emerging from the post-annealed analysis as shown in figures 4(c)) and (d). Firstly, approximately an order of magnitude reduction in both the tensile and compressive strain components is noted. Secondly, we note a drastic change in the overall local strain profile, indicating a diffusive-like strain relaxation mechanism (note differences in *x*-axis scale between the as implanted and annealed samples).

Work is ongoing in quantifying these variations as a function of lower implantation fluences and more sophisticated thermal treatments. Indeed, current efforts are aiming to build on this experiment in two key ways: 1) improving the quantitative model to account for more subtle effects, such as lattice tilting and reducing the background bulk SiC signal such that we can quantify the strain contributions down to an implantation fluence of ∼16 ions/spot, compatible with the synthesis of single color centers in 4H-SiC [71, 76, 77], and 2) quantifying and deconvolving the strain contributions as a function of various thermal processing schemes. Both of these efforts will be helped by reducing the relative interrogated volume of the implanted region vs the 4H-SiC bulk and the upcoming planned APS-U upgrades scheduled for 2023 that would greatly increase the x-ray fluence for such experiments. These advances promise to provide an intimate understanding of the formation dynamics of VV^0 in 4H-SiC while paving the way for deterministic synthesis of quantum relevant color-centers in technologically relevant material systems.

4. Summary and outlook

In summary, crystallographic features local to quantum spin defects result in varied strain profiles and reduced lattice symmetries, playing a significant role in the local electrostatic environments of said defects, often negatively affecting their optical properties and indistinguishability. An exhaustive investigation of such features at the relevant length scales of <1 μm would enable a better understanding of inter-qubit variability in the solid state, while paving the way for strain engineering and deterministic localization of a variety of spin defect systems.

The exact effects of these crystallographic features on the spin-defect to host-material relationship remains poorly understood due to the inherent complexity and local nature of these interplays. This has motivated the development of tools to both probe and generate such features. Specifically, single defect relevant nano-implantation capabilities have been demonstrated at the Center for Integrated Nanotechnologies at the Department of Energy's Sandia National Laboratories. Additionally, non-destructive local x-ray 3D strain imaging with nanoscale (∼25 nm) resolution has been demonstrated at the Hard x-ray Nanoprobe (HXN) of the Department of Energy's Advanced Photon Source (Argonne National Laboratory) and the Center for Nanoscale Materials. These versatile experimental platforms, available through the U.S. Department of Energy's Nanoscale Science Research Centers have enabled a number of recent advances in understanding the structural dependency of spin qubit/host systems and methods to improve and harness the local crystallographic environment of these quantum systems.

Utilizing these tools, we were able to demonstrate spatially deterministic creation of neutral divacancy centers in 4H-SiC, while investigating and characterizing these systems on the <25 nm scale with strain sensitivities relevant to begin to explore defect formation dynamics. From this, we were able to extract preliminary indicators of how annealing dynamics affect nano-implanted defects' local strain environments and by extension, their optical properties. These demonstrations lay the foundation of ongoing works on divacancy synthesis dynamics as a function of strain and thermal treatments. This is done in the context of studying single VV^0 formation in 4H-SiC from a strain and photoluminescence perspective as a means to achieve deterministic creation of low strain homogeneous quantum relevant spin defects in the solid state. Overall, this promises to enable scalability and integration of quantum and classical technologies by reducing the inherent variability, while increasing yield.

Acknowledgments

This material and effort is based upon work primarily supported by the U.S. Department of Energy Office of Science National Quantum Information Science Research Centers as part of the Q-NEXT center (ND, MH, DDA, and FJH). Additional support for preliminary measurements was funded by the U.S. Department of Energy, Office of Basic Energy Sciences, Materials Science and Engineering Division (SJW). This work was performed, in part, at the Center for Integrated Nanotechnologies, an Office of Science User Facility operated for the U.S. Department of Energy (DOE) Office of Science. Sandia National Laboratories is a multi-mission laboratory managed and operated by National Technology & Engineering Solutions of Sandia, LLC, a wholly owned subsidiary of Honeywell International, Inc., for the U.S. DOE's National Nuclear Security Administration under contract DE-NA-0003525. The views expressed in the article do not necessarily represent the views of the U.S. DOE or the United States Government. SLB acknowledges support from UK Research and Innovation [Grant: MR/W006928/1]. Work performed at the Center for Nanoscale Materials and Advanced Photon Source, both U.S. Department of Energy Office of Science User Facilities, was supported by the US DOE, Office of Basic Energy Sciences, under Contract No. DE-AC02-06CH11357.

Data availability statement

All data that support the findings of this study are included within the article (and any supplementary files). The data underlying this paper are available at DOI: https://doi.org/10.5281/zenodo.7706607.

Conflict of interest

All authors confirm that there are no conflicts of interest with this article.

ORCID iDs

Nazar Delegan https://orcid.org/0000-0002-1240-6409
Sam L Bayliss https://orcid.org/0000-0002-1156-7243

References

[1] Awschalom D D, Hanson R, Wrachtrup J and Zhou B B 2018 Quantum technologies with optically interfaced solid-state spins *Nat. Photon.* **12** 516–27
[2] Wolfowicz G, Heremans F J, Anderson C P, Kanai S, Seo H, Gali A, Galli G and Awschalom D D 2021 Quantum guidelines for solid-state spin defects *Nat. Rev. Mater.* **6** 906–25
[3] Gruber A, Dräbenstedt A, Tietz C, Fleury L, Wrachtrup J and Borczyskowski C von 1997 Scanning confocal optical microscopy and magnetic resonance on single defect centers *Science (80-)* **276** 2012–4
[4] Jelezko F, Gaebel T, Popa I, Domhan M, Gruber A and Wrachtrup J 2004 Observation of Coherent oscillation of a single nuclear spin and realization of a two-qubit conditional quantum gate *Phys. Rev. Lett.* **93** 130501
[5] Hanson R, Gywat O and Awschalom D D 2006 Room-temperature manipulation and decoherence of a single spin in diamond *Phys. Rev.* B **74** 161203
[6] Christle D J, Falk A L, Andrich P, Klimov P V, Hassan J U, Son N T, Janzén E, Ohshima T and Awschalom D D 2015 Isolated electron spins in silicon carbide with millisecond coherence times *Nat. Mater.* **14** 160–3
[7] Falk A L, Buckley B B, Calusine G, Koehl W F, Dobrovitski V V, Politi A, Zorman C A, Feng P X L and Awschalom D D 2013 Polytype control of spin qubits in silicon carbide *Nat. Commun.* **4** 1819
[8] Koehl W F, Buckley B B, Heremans F J, Calusine G and Awschalom D D 2011 Room temperature coherent control of defect spin qubits in silicon carbide *Nature* **479** 84–7
[9] Balasubramanian G *et al* 2009 Ultralong spin coherence time in isotopically engineered diamond *Nat. Mater.* **8** 383–7
[10] Maurer P C *et al* 2012 Room-Temperature quantum bit memory exceeding one second *Science (80-)* **336** 1283–6
[11] Herbschleb E D *et al* 2019 Ultra-long coherence times amongst room-temperature solid-state spins *Nat. Commun.* **10** 3766
[12] Miao K C, Blanton J P, Anderson C P, Bourassa A, Crook A L, Wolfowicz G, Abe H, Ohshima T, Awschalom D D and David D 2020 Universal coherence protection in a solid-state spin qubit *Science (80-)* **369** 1493–7
[13] Anderson C P *et al* 2022 Five-second coherence of a single spin with single-shot readout in silicon carbide *Sci. Adv.* **8** eabm5912
[14] Bradley C E, Randall J, Abobeih M H, Berrevoets R C, Degen M J, Bakker M A, Markham M, Twitchen D J and Taminiau T H 2019 A ten-qubit solid-state spin register with quantum memory up to one minute *Phys. Rev.* X **9** 031045
[15] Bourassa A *et al* 2020 Entanglement and control of single nuclear spins in isotopically engineered silicon carbide *Nat. Mater.* **19** 1319–25
[16] Bernien H *et al* 2013 Heralded entanglement between solid-state qubits separated by three metres *Nature* **497** 86–90
[17] Hensen B *et al* 2015 Loophole-free Bell inequality violation using electron spins separated by 1.3 kilometres *Nature* **526** 682–6
[18] Humphreys P C, Kalb N, Morits J P J, Schouten R N, Vermeulen R F L, Twitchen D J, Markham M and Hanson R 2018 Deterministic delivery of remote entanglement on a quantum network *Nature* **558** 268–73
[19] Nguyen M, Nikolay N, Bradac C, Kianinia M, Ekimov E A, Mendelson N, Benson O and Aharonovich I 2019 Photodynamics and quantum efficiency of germanium vacancy color centers in diamond *Adv. Photon.* **1** 1
[20] Barry J F, Schloss J M, Bauch E, Turner M J, Hart C A, Pham L M and Walsworth R L 2020 Sensitivity optimization for NV-diamond magnetometry *Rev. Mod. Phys.* **92** 015004
[21] Tallaire A, Kasu M, Ueda K and Makimoto T 2008 Origin of growth defects in CVD diamond epitaxial films *Diam. Relat. Mater.* **17** 60–5
[22] Knauer S, Hadden J P and Rarity J G 2020 In-situ measurements of fabrication induced strain in diamond photonic-structures using intrinsic colour centres *npj Quantum Inf.* **6** 50
[23] van Dam S B *et al* 2019 Optical coherence of diamond nitrogen-vacancy centers formed by ion implantation and annealing *Phys. Rev.* B **99** 161203
[24] Ruf M, IJspeert M, van Dam S, de Jong N, van den Berg H, Evers G and Hanson R 2019 Optically coherent nitrogen-vacancy centers in micrometer-thin etched diamond membranes *Nano Lett.* **19** 3987–92

[25] Löfgren R, Öberg S and Larsson J A 2022 The diamond NV-center transition energies in the vicinity of an intrinsic stacking fault *AIP Adv.* **12** 035009

[26] Körner W, Urban D F and Elsässer C 2021 Influence of extended defects on the formation energy, hyperfine structure, and zero-field splitting of NV centers in diamond *Phys. Rev.* B **103** 1–8

[27] Arnault J-C, Saada S and Ralchenko V 2022 Chemical vapor deposition single-crystal diamond: a review *Phys. Status Solidi—Rapid Res. Lett.* **16** 2100354

[28] La Via F, Camarda M and La Magna A 2014 Mechanisms of growth and defect properties of epitaxial SiC *Appl. Phys. Rev.* **1** 031301

[29] Harmon K J, Delegan N, Highland M J, He H, Zapol P, Heremans F J and Hruszkewycz S O 2022 Designing silicon carbide heterostructures for quantum information science: challenges and opportunities *Mater. Quantum Technol.* **2** 023001

[30] Sangtawesin S *et al* 2019 Origins of Diamond surface noise probed by correlating single-spin measurements with surface spectroscopy *Phys. Rev. X* **9** 031052

[31] Smith J M, Meynell S A, Bleszynski Jayich A C and Meijer J 2019 Colour centre generation in diamond for quantum technologies *Nanophotonics* **8** 1889–906

[32] de Leon N P, Itoh K M, Kim D, Mehta K K, Northup T E, Paik H, Palmer B S, Samarth N, Sangtawesin S and Steuerman D W 2021 Materials challenges and opportunities for quantum computing hardware *Science* **372** eabb2823

[33] Rodgers L V H, Hughes L B, Xie M, Maurer P C, Kolkowitz S, Bleszynski Jayich A C and de Leon N P 2021 Materials challenges for quantum technologies based on color centers in diamond *MRS Bull.* **46** 623–33

[34] Broadway D A *et al* 2019 Microscopic imaging of the stress tensor in diamond using in situ quantum sensors *Nano Lett.* **19** 4543–50

[35] McCullian B A, Cheung H F H, Chen H Y and Fuchs G D 2022 Quantifying the spectral diffusion of N- V centers by symmetry *Phys. Rev. Appl.* **18** 064011

[36] Doherty M W, Manson N B, Delaney P, Jelezko F, Wrachtrup J and Hollenberg L C L 2013 The nitrogen-vacancy colour centre in diamond *Phys. Rep.* **528** 1–45

[37] Biktagirov T B, Smirnov A N, Davydov V Y, Doherty M W, Alkauskas A, Gibson B C and Soltamov V A 2017 Strain broadening of the 1042 nm zero phonon line of the NV-center in diamond: a promising spectroscopic tool for defect tomography *Phys. Rev.* B **96** 1–7

[38] Christle D J *et al* 2017 Isolated spin qubits in SiC with a high-fidelity infrared spin-to-photon interface *Phys. Rev. X* **7** 021046

[39] Lee K W, Lee D, Ovartchaiyapong P, Minguzzi J, Maze J R and Bleszynski Jayich A C 2016 Strain coupling of a mechanical resonator to a single quantum emitter in diamond *Phys. Rev. Appl.* **6** 1–41

[40] Teissier J, Barfuss A, Appel P, Neu E and Maletinsky P 2014 Strain coupling of a nitrogen-vacancy center spin to a diamond mechanical oscillator *Phys. Rev. Lett.* **113** 1–5

[41] Barfuss A, Teissier J, Neu E, Nunnenkamp A and Maletinsky P 2015 Strong mechanical driving of a single electron spin *Nat. Phys.* **11** 820–4

[42] Jahn H A and Teller E 1937 Stability of polyatomic molecules in degenerate electronic states: I. Orbital degeneracy *Proc. R. Soc.* A **161** 220–35

[43] Ivády V *et al* 2019 Stabilization of point-defect spin qubits by quantum wells *Nat. Commun.* **10** 5607

[44] Christle D J *et al* 2017 Isolated spin qubits in SiC with a high-fidelity infrared spin-to-photon interface *Phys. Rev. X* **7** 1–12

[45] Crook A L *et al* 2020 Purcell enhancement of a single silicon carbide color center with coherent spin control *Nano Lett.* **20** 3427–34

[46] Anderson C P *et al* 2019 Electrical and optical control of single spins integrated in scalable semiconductor devices *Science (80-)* **1230** 1225–30

[47] Doherty M W, Manson N B, Delaney P and Hollenberg L C L 2011 The negatively charged nitrogen-vacancy centre in diamond: the electronic solution *New J. Phys.* **13** 025019

[48] Whiteley S J *et al* 2019 Spin–phonon interactions in silicon carbide addressed by Gaussian acoustics *Nat. Phys.* **15** 490–5

[49] De Las Casas C F, Christle D J, Ul Hassan J, Ohshima T, Son N T and Awschalom D D 2017 Stark tuning and electrical charge state control of single divacancies in silicon carbide *Appl. Phys. Lett.* **111** 262403

[50] Hsieh S *et al* 2019 Imaging stress and magnetism at high pressures using a nanoscale quantum sensor *Science* **366** 1349–54

[51] Liu L *et al* 2022 Coherent control and magnetic detection of divacancy spins in silicon carbide at high pressures *Nano Lett.* **22** 9943–50

[52] Whiteley S J, Heremans F J, Wolfowicz G, Awschalom D D and Holt M V 2019 Correlating dynamic strain and photoluminescence of solid-state defects with stroboscopic x-ray diffraction microscopy *Nat. Commun.* **10** 3386

[53] Holt M, Harder R, Winarski R and Rose V 2013 Nanoscale hard x-ray microscopy methods for materials studies *Annu. Rev. Mater. Res.* **43** 183–211

[54] Marshall M C, Phillips D F, Turner M J, Ku M J H, Zhou T, Delegan N, Heremans F J, Holt M V and Walsworth R L 2021 Scanning x-ray diffraction microscopy for diamond quantum sensing *Phys. Rev. Appl.* **16** 054032

[55] Tamarat P *et al* 2006 Stark shift control of single optical centers in diamond *Phys. Rev. Lett.* **97** 083002

[56] Tallaire A, Brinza O, Mille V, William L and Achard J 2017 Reduction of dislocations in single crystal diamond by lateral growth over a macroscopic hole *Adv. Mater.* **29** 1604823

[57] Leone S, Henry A, Janzén E and Nishizawa S 2013 Epitaxial growth of SiC with chlorinated precursors on different off-angle substrates *J. Cryst. Growth* **362** 170–3

[58] Stahlbush R E, VanMil B L, Myers-Ward R L, Lew K-K, Gaskill D K and Eddy C R 2009 Basal plane dislocation reduction in 4H-SiC epitaxy by growth interruptions *Appl. Phys. Lett.* **94** 041916

[59] Udvarhelyi P, Shkolnikov V O, Gali A, Burkard G and Pályi A 2018 Spin-strain interaction in nitrogen-vacancy centers in diamond *Phys. Rev.* B **98** 075201

[60] Ebadi R *et al* 2022 Directional detection of dark matter using solid-state quantum sensing *AVS Quantum Sci.* **4** 044701

[61] Bassett L C, Heremans F J, Yale C G, Buckley B B and Awschalom D D 2011 Electrical tuning of single nitrogen-vacancy center optical transitions enhanced by photoinduced fields *Phys. Rev. Lett.* **107** 1–5

[62] Chen D, Zheludev N and Gao W 2020 Building blocks for quantum network based on group-iv split-vacancy centers in diamond *Adv. Quantum Technol.* **3** 1900069

[63] Meesala S *et al* 2018 Strain engineering of the silicon-vacancy center in diamond *Phys. Rev.* B **97** 1–13

[64] Sohn Y I *et al* 2018 Controlling the coherence of a diamond spin qubit through its strain environment *Nat. Commun.* **9** 17–22

[65] Maity S, Shao L, Sohn Y I, Meesala S, Machielse B, Bielejec E, Markham M and Lončar M 2018 Spectral alignment of single-photon emitters in diamond using strain gradient *Phys. Rev. Appl.* **10** 1–7

[66] Hruszkewycz S O, Allain M, Holt M V, Murray C E, Holt J R, Fuoss P H and Chamard V 2017 High-resolution three-dimensional structural microscopy by single-angle bragg ptychography *Nat. Mater.* **16** 244–51

[67] Hruszkewycz S O, Highland M J, Holt M V, Kim D, Folkman C M, Thompson C, Tripathi A, Stephenson G B, Hong S and Fuoss P H 2013 Imaging local polarization in ferroelectric thin films by coherent X-ray bragg projection ptychography *Phys. Rev. Lett.* **110** 1–5

[68] Titze M, Byeon H, Flores A, Henshaw J, Harris C T, Mounce A M and Bielejec E S 2022 In situ ion counting for improved implanted ion error rate and silicon vacancy yield uncertainty *Nano Lett.* **22** 3212–8

[69] Carlos W E, Garces N Y, Glaser E R and Fanton M A 2006 Annealing of multivacancy defects in 4H-SiC *Phys. Rev.* B **74** 235201

[70] Almutairi A F M, Partridge J G, Xu C, Cole I S and Holland A S 2022 Direct writing of divacancy centers in silicon carbide by femtosecond laser irradiation and subsequent thermal annealing *Appl. Phys. Lett.* **120** 014003

[71] Pavunny S P, Yeats A L, Banks H B, Bielejec E, Myers-Ward R L, DeJarld M T, Bracker A S, Gaskill D K and Carter S G 2021 Arrays of Si vacancies in 4H-SiC produced by focused Li ion beam implantation *Sci. Rep.* **11** 3561

[72] Zolnai Z, Son N T, Hallin C and Janzén E 2004 Annealing behavior of the carbon vacancy in electron-irradiated 4H-SiC *J. Appl. Phys.* **96** 2406–8

[73] Son N T *et al* 2006 Divacancy in 4H-SiC *Phys. Rev. Lett.* **96** 055501

[74] Dietz J R and Hu E L 2022 Optical and strain stabilization of point defects in silicon carbide *Appl. Phys. Lett.* **120** 184001

[75] Als-Nielsen J and McMorrow D 2011 *Elements of Modern X-ray Physics* (New York: Wiley)

[76] Kraus H *et al* 2017 Three-dimensional proton beam writing of optically active coherent vacancy spins in silicon carbide *Nano Lett.* **17** 2865–70

[77] Wang J *et al* 2017 Scalable fabrication of single silicon vacancy defect arrays in silicon carbide using focused ion beam *ACS Photon.* **4** 1054–9